

# Regulated degradation of HMG CoA reductase requires conformational changes in sterol-sensing domain

Received: 12 June 2022

Accepted: 12 July 2022

Published online: 25 July 2022

 Check for updates

Hongwen Chen<sup>1,3</sup>, Xiaofeng Qi<sup>1,3</sup>, Rebecca A. Faulkner<sup>1</sup>,  
Marc M. Schumacher<sup>1</sup>, Linda M. Donnelly<sup>1</sup>, Russell A. DeBose-Boyd<sup>1</sup>✉ &  
Xiaochun Li<sup>1,2</sup>✉

3-Hydroxy-3-methylglutaryl coenzyme A reductase (HMGR) is the rate-limiting enzyme in cholesterol synthesis and target of cholesterol-lowering statin drugs. Accumulation of sterols in endoplasmic reticulum (ER) membranes accelerates degradation of HMGR, slowing the synthesis of cholesterol. Degradation of HMGR is inhibited by its binding to UBIAD1 (UbiA prenyltransferase domain-containing protein-1). This inhibition contributes to statin-induced accumulation of HMGR, which limits their cholesterol-lowering effects. Here, we report cryo-electron microscopy structures of the HMGR-UBIAD1 complex, which is maintained by interactions between transmembrane helix (TM) 7 of HMGR and TMs 2–4 of UBIAD1. Disrupting this interface by mutagenesis prevents complex formation, enhancing HMGR degradation. TMs 2–6 of HMGR contain a 170-amino acid sterol sensing domain (SSD), which exists in two conformations—one of which is essential for degradation. Thus, our data supports a model that rearrangement of the TMs in the SSD permits recruitment of proteins that initiate HMGR degradation, a key reaction in the regulatory system that governs cholesterol synthesis.

3-Hydroxy-3-methylglutaryl coenzyme A reductase (HMGR) is a polytopic, endoplasmic reticulum (ER)-localized glycoprotein that catalyzes a rate-limiting step in synthesis of cholesterol and essential nonsterol isoprenoids such as farnesyl pyrophosphate and geranylgeranyl pyrophosphate (GGpp)<sup>1</sup>. HMGR is tightly controlled by a complex feedback regulatory system that allows cells to constantly synthesize nonsterol isoprenoids while avoiding toxic overproduction of cholesterol and other sterols<sup>2–5</sup>. Part of this feedback control involves accelerated ERAD (ER-associated degradation) of HMGR<sup>6,7</sup>. This ERAD is initiated by the accumulation of sterols in ER membranes, which triggers binding of HMGR to ER membrane proteins called Insigs<sup>8,9</sup>. Insig binding is mediated by the N-terminal membrane domain of HMGR, which is both necessary and sufficient for ERAD and contains eight transmembrane helices (TMs) that precede a large

cytosolic catalytic domain<sup>10,11</sup>. TMs 2–6 of HMGR comprise what is known as the sterol-sensing domain (SSD); mutation of a tetrapeptide sequence (Y<sub>75</sub>IYF) in the SSD of HMGR abolishes its binding to Insigs, preventing ubiquitination and ERAD<sup>9</sup>. Insig-associated ubiquitin ligases mediate ubiquitination of lysines-89 and -248 (K89 and K248), which are exposed to the cytosol and lie adjacent to TMs 3 and 7 of HMGR, respectively<sup>9,12–14</sup>. Sterol-induced ubiquitination marks HMGR for extraction across ER membranes, after which it becomes dislocated into the cytosol for proteasomal degradation<sup>15</sup>. The combination of K89R and K248R mutations prevent sterol-induced ubiquitination and ERAD of HMGR in both cultured cells and tissues of knock-in mice<sup>9,16</sup>.

Whereas Insigs accelerate the ERAD of HMGR, another protein called UBIAD1 (UbiA prenyltransferase domain-containing protein-1)

<sup>1</sup>Department of Molecular Genetics, University of Texas Southwestern Medical Center, Dallas, TX, USA. <sup>2</sup>Department of Biophysics, University of Texas Southwestern Medical Center, Dallas, TX, USA. <sup>6</sup>These authors contributed equally: Hongwen Chen, Xiaofeng Qi.

✉ e-mail: [russell.debose-boyd@utsouthwestern.edu](mailto:russell.debose-boyd@utsouthwestern.edu); [xiaochun.li@utsouthwestern.edu](mailto:xiaochun.li@utsouthwestern.edu)

binds to and stabilizes the enzyme<sup>17,18</sup>. UBIAD1 was discovered as the enzyme that transfers the geranylgeranyl group from GGpp to menadiolone producing the vitamin K<sub>2</sub> subtype menaquinone-4 (MK-4)<sup>19,20</sup>. We subsequently identified UBIAD1 as a GGpp sensor that binds to HMGR and inhibits its ERAD when ER membranes are depleted of GGpp<sup>17</sup>. When GGpp accumulates within ER membranes, the isoprene binds to UBIAD1, causing it to dissociate from HMGR and translocate to the medial-*trans* cisternae of the Golgi<sup>17,21</sup>. Importantly, GGpp-induced translocation of UBIAD1 from the ER-to-Golgi occurs in HMGR-deficient cells<sup>22</sup>. Dissociation from UBIAD1 allows for the maximal ERAD of HMGR (Fig. 1a). The physiologic significance of the UBIAD1-HMGR interaction is confirmed by the observation that missense mutations in UBIAD1 cause Schnyder corneal dystrophy (SCD), an

autosomal-dominant eye disease characterized by corneal opacification owing to the over-accumulation of cholesterol<sup>23,24</sup>. SCD-associated variants of UBIAD1 are sequestered in the ER and resist GGpp-induced dissociation from HMGR (Fig. 1a). As a result, SCD-associated UBIAD1 inhibits ERAD of HMGR, which leads to enhanced synthesis and accumulation of cholesterol in both cultured cells and tissues of mice<sup>17,21,22,25</sup>.

Competitive inhibitors of HMGR called statins are prescribed to lower circulating levels of low density lipoprotein (LDL)-cholesterol and reduce the incidence of atherosclerotic cardiovascular disease (ACVD)<sup>26,27</sup>. However, the efficacy of statins is reduced because they disrupt feedback control of HMGR owing to depletion of sterol and nonsterol isoprenoids (including GGpp). This depletion leads to the

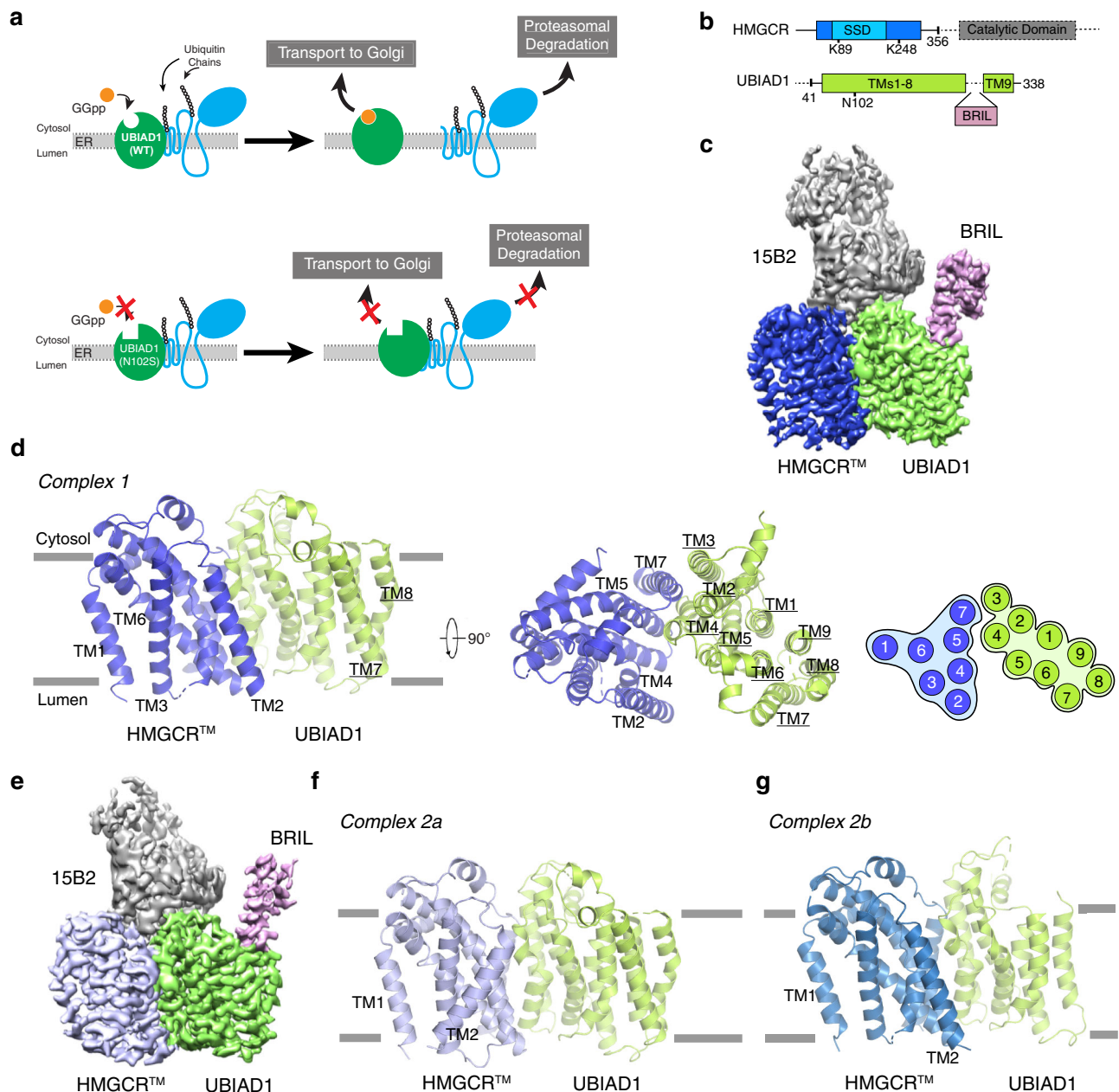


**Fig. 1 | Cryo-EM structure of the HMGR<sup>TM</sup>-UBIAD1<sup>N102S</sup> complex.** **a** Overview of UBIAD1-mediated regulation of HMGR ERAD. **b** Schematic representation of HMGR and UBIAD1 variants used for structural determination. The position of BRIL insertion in UBIAD1 is indicated. **c** Cryo-EM map of HMGR<sup>TM</sup>-UBIAD1<sup>N102S</sup> complex 1. **d** Overall structure of HMGR<sup>TM</sup>-UBIAD1<sup>N102S</sup> complex 1 viewed from the

side of the membrane (left) and cytosol (right). The TMs of UBIAD1 are denoted by underlining. The cartoon denotes a slice of the TMs of HMGR<sup>TM</sup> and UBIAD1<sup>N102S</sup> with helices indicated by numbers. **e** Cryo-EM map of HMGR<sup>TM</sup>-UBIAD1<sup>N102S</sup> complex 2a. **f, g** Overall structure of HMGR<sup>TM</sup>-UBIAD1<sup>N102S</sup> complex 2a **f** and complex 2b **g** viewed from the membrane side.

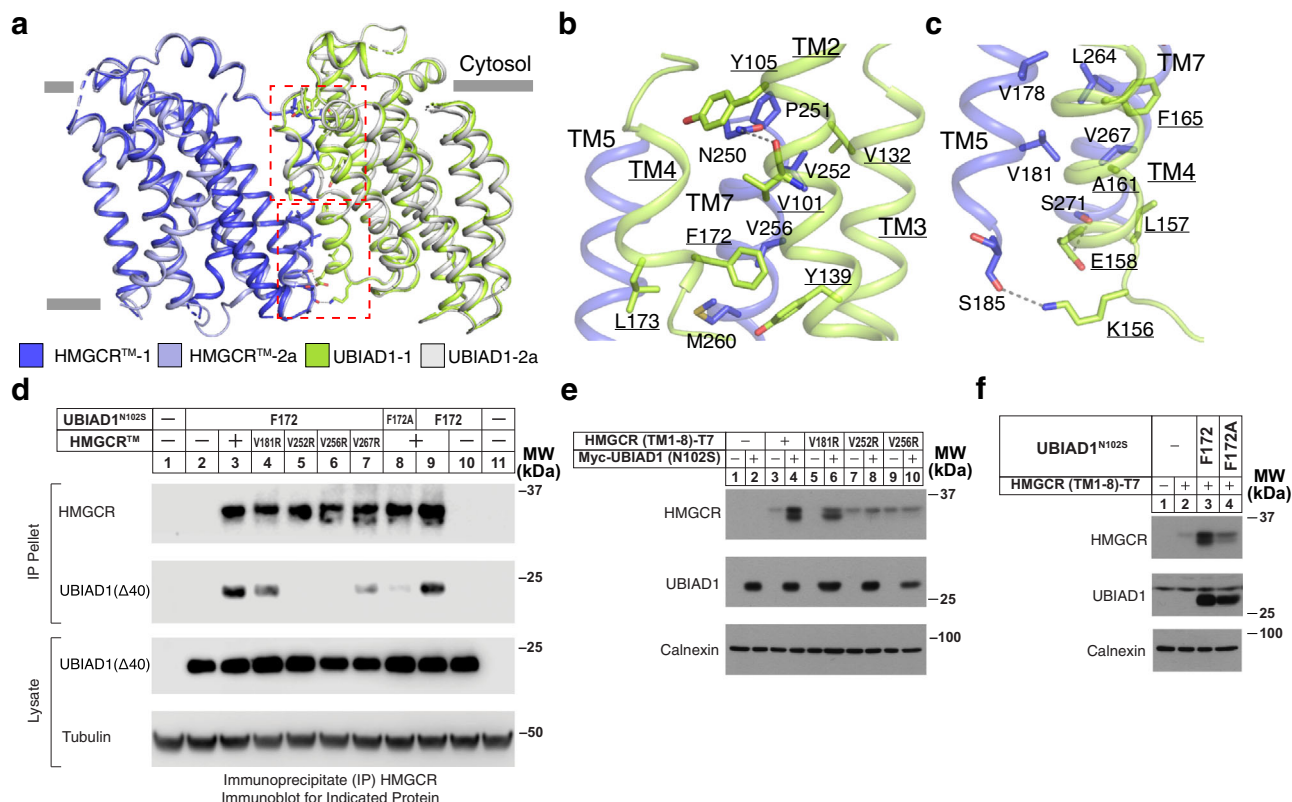


**Fig. 2 | Analysis of the HMGCR<sup>TM</sup>-UBIAD1<sup>N102S</sup> complex interface.** **a** Structural comparison of HMGCR<sup>TM</sup>-UBIAD1<sup>N102S</sup> complex 1 and complex 2a. HMGCR-TM2 adopts distinct conformations in the two complexes. TMs that comprise the interface of the HMGCR-UBIAD1 are indicated dashed red boxes. Detailed interactions in the upper and lower dashed boxes are shown individually in **b**, **c**, respectively. Residues that contribute to complex formation are labeled; hydrophilic interactions are indicated by dashed lines. **d** Detergent lysates of HEK-293 GnTI cells transfected with expression plasmids encoding FLAG-tagged HMGCR<sup>TM</sup> and Strep-tagged UBIAD1<sup>N102S</sup> were precipitated with anti-FLAG-M2

agarose beads. Aliquots of resulting precipitates and lysates were subjected to SDS-PAGE, followed by immunoblot analysis. Experimental details are provided in “Methods”. **e**, **f** SV-589 (ΔUBIAD1) cells transfected with expression plasmids encoding indicated variant of HMGCR (TM1-8)-T7 and Myc-UBIAD1 (N102S) were lysed and subjected to subcellular fractionation. Aliquots of resulting membrane fractions were then subjected to SDS-PAGE and immunoblot analysis with anti-FLAG or anti-T7 (for HMGCR) and anti-Strep or anti-Myc (IgG-9E10, for UBIAD1). Additional experimental details can be found in “Methods”. Source data are provided as a Source Data file.

accumulation of HMGCR in the liver that overcomes inhibitory effects of statins, allowing continued synthesis of cholesterol that limits lowering of plasma cholesterol<sup>28–32</sup>. Our previous studies indicated that inhibition of ERAD substantially contributes to statin-induced accumulation of HMGCR, which correlates with ER sequestration of UBIAD1<sup>16,25</sup>. However, the molecular basis through which sterols and GGpp accelerate ERAD of HMGCR and how UBIAD1 blocks the reaction is unknown. Here, we determined cryogenic electron microscopy (cryo-EM) structures of HMGCR bound to SCD-associated UBIAD1 (N102S). Structural and functional analysis provide key insights into mechanisms for UBIAD1-mediated protection of HMGCR from ERAD. These findings have important implications for development of agents that enhance statin efficacy and further reduce ACVD. Moreover, our studies reveal that the HMGCR SSD adopts a specific conformation required for sterol-accelerated ERAD, establishing the molecular basis through which the region mediates regulation of cholesterol synthesis.

## Results

### Assembly of a complex between HMGCR and UBIAD1

We focused on the stabilizing interaction between the membrane domain of hamster HMGCR and UBIAD1. The hamster proteins share over 95% overall identity with their human counterparts (Supplementary Fig. 1). Expression plasmids were prepared that encode the FLAG-tagged membrane domain of HMGCR harboring arginine substitutions for K89 and K248 (designated HMGCR<sup>TM</sup>) and Strep-tagged UBIAD1 from which we deleted a flexible N-terminal region (amino acids 1–40).

We included the SCD-associated N102S mutation, which blunts enzymatic activity<sup>20,33</sup>; this protein is designated UBIAD1<sup>N102S</sup> (Fig. 1b). Notably, UBIAD1 containing the N-terminal deletion continued to localize to the Golgi of GGpp-replete cells (Supplementary Fig. 2), indicating the protein was normally folded. HMGCR<sup>TM</sup> and UBIAD1<sup>N102S</sup> were co-expressed in HEK-293 GnTI cells and purified by anti-FLAG chromatography. Gel filtration shows that the HMGCR<sup>TM</sup>-UBIAD1<sup>N102S</sup> complex migrated as a single peak (Supplementary Fig. 3a); the presence of both proteins in the peak fraction was confirmed by immunoblot and mass spectrometry. Unfortunately, cryo-EM images of the HMGCR<sup>TM</sup>-UBIAD1<sup>N102S</sup> complex displayed limited features and we failed to reconstitute a 3D model.

Hydropathy plots predict that UBIAD1 is comprised of 9 TMs. To provide a fiducial marker for particle image alignment in cryo-EM structure determination, we inserted the soluble, thermostabilized apocytochrome b562RIL (BRIL)<sup>34</sup> in a cytosolic loop predicted to localize between TMs 8 and 9 of UBIAD1 (designated UBIAD1-BRIL<sup>N102S</sup>) (Fig. 1b). The yield and biochemical stability of the HMGCR<sup>TM</sup>-UBIAD1-BRIL<sup>N102S</sup> was considerably enhanced compared to the HMGCR<sup>TM</sup>-UBIAD1<sup>N102S</sup> complex. HMGCR<sup>TM</sup>-UBIAD1-BRIL<sup>N102S</sup> was assembled into complex with anti-BRIL Fab (Fab<sup>BRIL</sup>)<sup>34</sup> and an anti-Fab nanobody (Nb)<sup>35</sup> in amphipols (Supplementary Fig. 3c, d), of which the structure was determined by cryo-EM at a resolution of 3.6-Å (Supplementary Fig. 4). Densities of all 9 TMs of UBIAD1 and TMs 1–7 of HMGCR were resolved. However, the cryo-EM map of HMGCR part does not provide sufficient resolution to determine the atomic structure (Supplementary Fig. 4c).

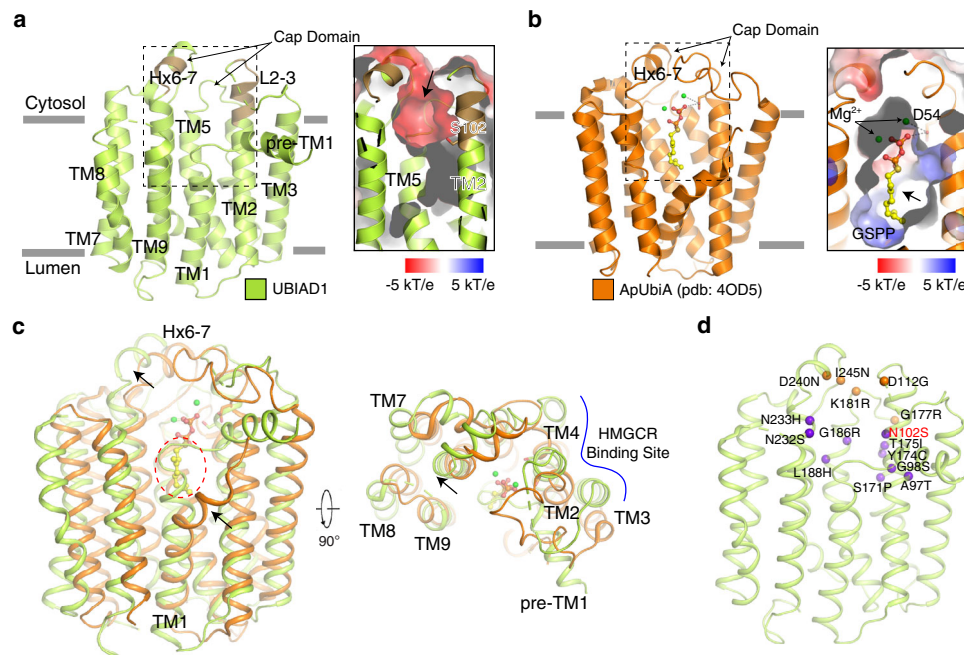


**Fig. 3 | Structural analysis of UBIAD1<sup>N102S</sup>.** **a** Overall structure of UBIAD1 viewed from the side of the membrane. N<sub>102</sub>TYYDFSKG and D<sub>236</sub>MESD motifs are colored in brown and cytosolic loops that form the Cap Domain are indicated by arrows. The electrostatic surface representation of the catalytic cavity is shown on the right. The entrance of the catalytic cavity is indicated by an arrow. The N102S mutation is shown in sticks. **b** Overall structure of the UbiA homolog from *Aeropyrum pernix* (ApUbiA) viewed from the side of the membrane. The electrostatic surface representation of the catalytic cavity is shown on the right. The entrance of the catalytic

cavity is indicated by an arrow. The putative substrate GSPP is shown in sticks and the Mg<sup>2+</sup> ions are shown in green balls. **c** Structural comparison of UBIAD1 and ApUbiA. The movements of TM1 and Hx6-7 are indicated by arrows. The potential clash between UBIAD1-TM1 and GSPP is indicated by a dashed oval. The HMGCRCR binding site is indicated by a blue line. **d** Distribution of SCD-associated mutation in UBIAD1. The mutations that locate in the cap domain are colored in orange and the mutations that locate in the catalytic core are colored in purple.

To address this problem, we generated and screened ~1000 hybridoma clones for conformation-specific antibodies using HMGCRCR<sup>TM</sup>-UBIAD1<sup>N102S</sup> complex as antigen. We identified one monoclonal antibody designated IgG-15B2 that bound native HMGCRCR<sup>TM</sup>-UBIAD1<sup>N102S</sup>, and found that BRIL insertion did not interfere the epitope recognition. Fab<sup>15B2</sup>, a Fab fragment derived from IgG-15B2, was co-purified with HMGCRCR<sup>TM</sup>-UBIAD1-BRIL<sup>N102S</sup> upon gel filtration (Supplementary Fig. 3b, e).

The structure of the HMGCRCR<sup>TM</sup>-UBIAD1-BRIL<sup>N102S</sup>-Fab<sup>15B2</sup> complex was determined by cryo-EM at a resolution of 3.3-Å (Fig. 1c, g, Supplementary Table 1). HMGCRCR<sup>TM</sup>-UBIAD1-BRIL<sup>N102S</sup>-Fab<sup>15B2</sup> complex existed as either a monomeric or dimeric heterotrimer. We observed clear densities for all 9 TMs of UBIAD1 and TMs 1-7 of HMGCRCR in the monomeric HMGCRCR<sup>TM</sup>-UBIAD1-BRIL<sup>N102S</sup>-Fab<sup>15B2</sup> heterotrimer (designated UBIAD1-HMGCRCR complex 1) (Fig. 1c, d, Supplementary Figs. 5, 6). Interestingly, within the dimeric structure of the HMGCRCR<sup>TM</sup>-UBIAD1-BRIL<sup>N102S</sup>-Fab<sup>15B2</sup> heterotrimer, each HMGCRCR<sup>TM</sup> in the complex existed in a different conformational state. The structure of one state, designated UBIAD1-HMGCRCR complex 2a, was determined at a resolution similar to that of complex 1 (Fig. 1f, Supplementary Figs. 5, 7). The structure of the other state, designated UBIAD1-HMGCRCR complex 2b, was resolved at a lower resolution. We observed clear cryo-EM map for TM1-7 of HMGCRCR in complex 2b (Supplementary Fig. 7a); however, maps corresponding to TMs 7-9 of UBIAD1, BRIL, and Fab<sup>15B2</sup> failed to be observed. The cryo-EM map shows that the HMGCRCR<sup>TM</sup>-UBIAD1-BRIL<sup>N102S</sup>-Fab<sup>15B2</sup> complex 2b was rotated 180° in detergent compared to complex 2a (Supplementary Fig. 7a). This rotation is likely an artifact of detergent solubilization and unlikely to be physiological.

### Overall Structure of the UBIAD1-HMGCRCR complex

Cryo-EM maps revealed that the Fab<sup>15B2</sup> epitope encompasses the cytosolic interface of the HMGCRCR<sup>TM</sup>-UBIAD1-BRIL<sup>N102S</sup> complex and

includes regions of both proteins (Fig. 1c, e, Supplementary Fig. 8). The possibility exists that Fab<sup>15B2</sup> modulates complex formation by altering the structure of HMGCRCR<sup>TM</sup> and/or UBIAD1-BRIL<sup>N102S</sup>. Structural analysis of HMGCRCR<sup>TM</sup>-UBIAD1-BRIL<sup>N102S</sup>-Fab<sup>15B2</sup> complex indicates that Fab<sup>BRIL</sup> and Nb disrupted the dimer interface (Supplementary Fig. 9a, b); thus, the HMGCRCR<sup>TM</sup>-UBIAD1-BRIL<sup>N102S</sup>-Fab<sup>BRIL</sup>-Nb complex was only observed in the monomeric state. Although the overall resolution of HMGCRCR<sup>TM</sup>-UBIAD1-BRIL<sup>N102S</sup>-Fab<sup>BRIL</sup>-Nb complex is lower than that of the HMGCRCR<sup>TM</sup>-UBIAD1-BRIL<sup>N102S</sup>-Fab<sup>15B2</sup> complex, structural analysis revealed the UBIAD1-HMGCRCR interface was identical in both complexes (Supplementary Figs. 4 and 9c).

The conformation of UBIAD1 is identical in Complexes 1 and 2a (Fig. 2a). The interface between UBIAD1 and HMGCRCR occupies an area of ~1000 Å<sup>2</sup>; the complex is maintained by several interactions between TMs 2 and 4 of UBIAD1 and TMs 5 and 7 of HMGCRCR (Figs. 1d and 2a). The main chain of V101, which localizes to TM2 of UBIAD1, makes hydrophilic contact with N250 in TM7 of HMGCRCR (Fig. 2b). TM4 of UBIAD1 makes additional hydrophobic contacts with HMGCRCR and two hydrophilic interactions are observed between E158 of UBIAD1-TM4 and S271 of HMGCRCR-TM7 and between K156 of UBIAD1-TM4 and the main chain in S185 of HMGCRCR-TM5 (Fig. 2c). A hydrophobic interface is formed by interaction of residues in TMs 5 and TM7 of HMGCRCR with residues in TM2, TM3, and TM4 of UBIAD1 (Fig. 2b, c).

We next compared the association of UBIAD1<sup>N102S</sup> with HMGCRCR<sup>TM</sup> and variants of the protein harboring mutations in the HMGCRCR-UBIAD1 interface predicted to disrupt complex formation (V181R, V252R, V256R, and V267R in HMGCRCR) (Fig. 2b, c). Because the HMGCRCR-UBIAD1 complex cannot be assembled in vitro, we used co-immunoprecipitation of the proteins expressed in vivo to measure their association. HEK-293 GnTI cells transfected with expression plasmids encoding Strep-tagged UBIAD1<sup>N102S</sup> and FLAG-tagged HMGCRCR<sup>TM</sup> or its variants were lysed and precipitated with anti-FLAG-

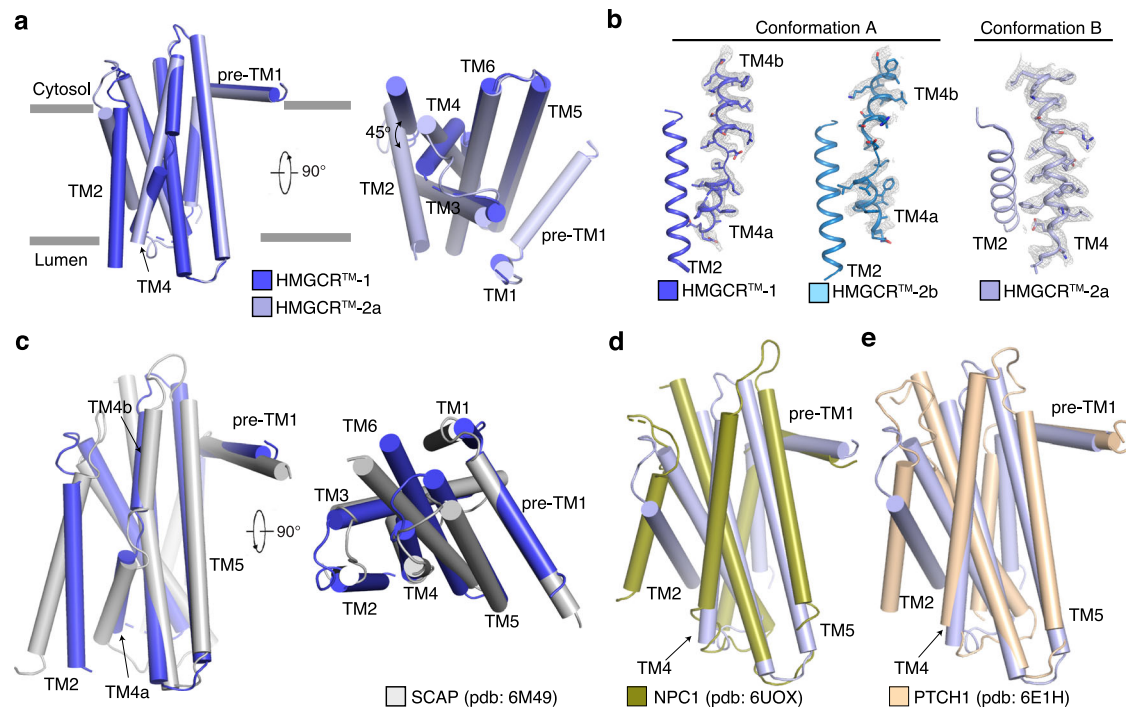


**Fig. 4 | Structural analysis of HMGCR<sup>TM</sup>.** **a** Structural comparison of HMGCR<sup>TM</sup>-1 and HMGCR<sup>TM</sup>-2a viewed from the side of the membrane (left) and lumen (right). **b** Structures of HMGCR-TM2 and TM4 in HMGCR<sup>TM</sup>-UBIAD1<sup>N102S</sup> complexes 1, 2a and 2b. The cryo-EM maps of TM4 are shown as gray mesh. **c–e** Structural

comparison of HMGCR-TMs 1–6 (Conformation A) to SCAP-TMs 1–6 **c**, HMGCR-TMs 1–6 (Conformation B) to NPC1-TMs 2–7 **d**, and HMGCR-TMs 1–6 (Conformation B) to PTCH1-TMs 1–6 **e**. HMGCR-TM4 is indicated by arrows.

coupled agarose beads. Immunoblot analysis of precipitated material revealed that as expected, UBIAD1<sup>N102S</sup> co-precipitated with HMGCR<sup>TM</sup> (Fig. 2d, lane 3). In contrast, UBIAD1<sup>N102S</sup> failed to be co-precipitated with HMGCR<sup>TM</sup> (V252R) and HMGCR<sup>TM</sup> (V256R) (lanes 5 and 6); HMGCR<sup>TM</sup> (V181R) and HMGCR<sup>TM</sup> (V267R) precipitated UBIAD1<sup>N102S</sup> albeit at slightly reduced levels compared to HMGCR<sup>TM</sup> (lanes 4 and 7). We also generated a variant of UBIAD1<sup>N102S</sup> containing a point mutation (F172A) at the HMGCR-UBIAD1 complex interface (Fig. 2b, c). The results show that co-precipitation of UBIAD1<sup>N102S</sup> (F172A) with HMGCR<sup>TM</sup> was reduced compared to UBIAD1<sup>N102S</sup> (compare lane 8 with lanes 3 and 9).

When transfected into UBIAD1-deficient cells, the amount of the T7-tagged membrane domain of wild type HMGCR (HMGCR (TM1-8)-T7) was low (Fig. 2e, lane 3). This is consistent with our previous observation that in both cultured cells and whole animals, ERAD of HMGCR was accelerated in the absence of UBIAD1<sup>21,36</sup>. Co-expression of full-length, Myc-tagged UBIAD1<sup>N102S</sup> markedly stabilized HMGCR (TM1-8)-T7 as expected (Fig. 2e, lane 4). HMGCR<sup>V181R</sup> (TM1-8)-T7 was similarly stabilized in the presence of Myc-UBIAD1<sup>N102S</sup> (Fig. 2e, lanes 5 and 6). However, HMGCR<sup>V252R</sup> (TM1-8)-T7 and HMGCR<sup>V256R</sup> (TM1-8)-T7 failed to become stabilized in the presence of Myc-UBIAD1<sup>N102S</sup> (Fig. 2e, lanes 7–10). Our structural observations were further supported by the finding that UBIAD1 (N102S/F172A) failed to stabilize HMGCR (TM1-8)-T7 to the extent observed with Myc-UBIAD1 (N102S) (Fig. 2f, lanes 3 and 4).

### Structural analysis of UBIAD1<sup>N102S</sup>

Despite limited sequence similarities, the overall structure of hamster UBIAD1<sup>N102S</sup> resembles the previously reported structures of two archaeal UbiA prenyltransferases<sup>37,38</sup> with a root-mean-square-deviation (RMSD) of 3.1 Å (Fig. 3a–c). Loops that separate the TM helices are relatively short except for the loop between TMs 2 and 3 (L2-3; amino acids 108–129) and the helix between TMs 6 and 7 (Hx6-7; amino acids 235–243). UbiA prenyltransferases contain two aspartate-rich motifs (NDXXDXXD and DXXD) that are essential for enzymatic activity<sup>39</sup>.

These motifs, which correspond to N<sub>102</sub>TYDFSKG and D<sub>236</sub>MESD in UBIAD1, are located at the C-terminal ends of TMs 2 and 6, respectively (Fig. 3a). Hx6-7, L2-3, and the loop between TMs 4 and 5 (L4-5) form a cap domain that lies over a central, negatively charged cavity generated by TMs 1, 2, 4, 5, and 6 (Fig. 3a). The structural analysis of the archaeal UbiA prenyltransferases suggests a model in which the cap domain adopts an open conformation in the absence of the isoprenyl substrate<sup>37,38</sup>. Binding of the substrate induces conformational changes in L2-3 that causes the cap domain to adopt a closed conformation that seals the enzyme's active site (Fig. 3b). The structure of UBIAD1<sup>N102S</sup> reveals that the cap domain adopts an open conformation, which is consistent with previous findings that the N102S mutation reduces the affinity of UBIAD1 for GGpp<sup>20</sup>. Figure 3d shows the location of residues in UBIAD1 that are mutated in SCD. SCD-associated mutations cluster in L2-3 and Hx6-7 or line the central cavity that harbors the enzyme's active site. These residues, many of which are conserved in UbiA prenyltransferases, are likely involved in binding of GGpp or catalysis. Indeed, our group and others have demonstrated that introduction of SCD-associated mutations in UBIAD1 reduces enzymatic activity<sup>20,33</sup>.

In comparing the structures of archaeal UbiA prenyltransferases (bound to substrate) and UBIAD1<sup>N102S</sup>, we noticed a significant difference. The central cavity in the archaeal enzymes has a lateral opening delineated by kinked TM1 and TM9<sup>38</sup> (Fig. 3b, c). This lateral opening may allow these enzymes to accommodate longer isoprenyl substrates and/or release reaction products. Interestingly, TM1 of UBIAD1<sup>N102S</sup> forms an intact  $\alpha$ -helix that blocks the lateral opening (Fig. 3a, c). It is tempting to speculate that binding to GGpp or MK-4 triggers conformational changes in TM1 that allows release of the product into the membrane bilayer.

### Structural analysis of HMGCR<sup>TM</sup>

The overall structure of HMGCR<sup>TM</sup> revealed that TMs1–7 are integrated into membranes. The loops between TM1 and TM2 (25 amino acids in length) as well as TM8 were not visualized in the structure, which indicates considerable flexibility within the regions (Fig. 1d). Further

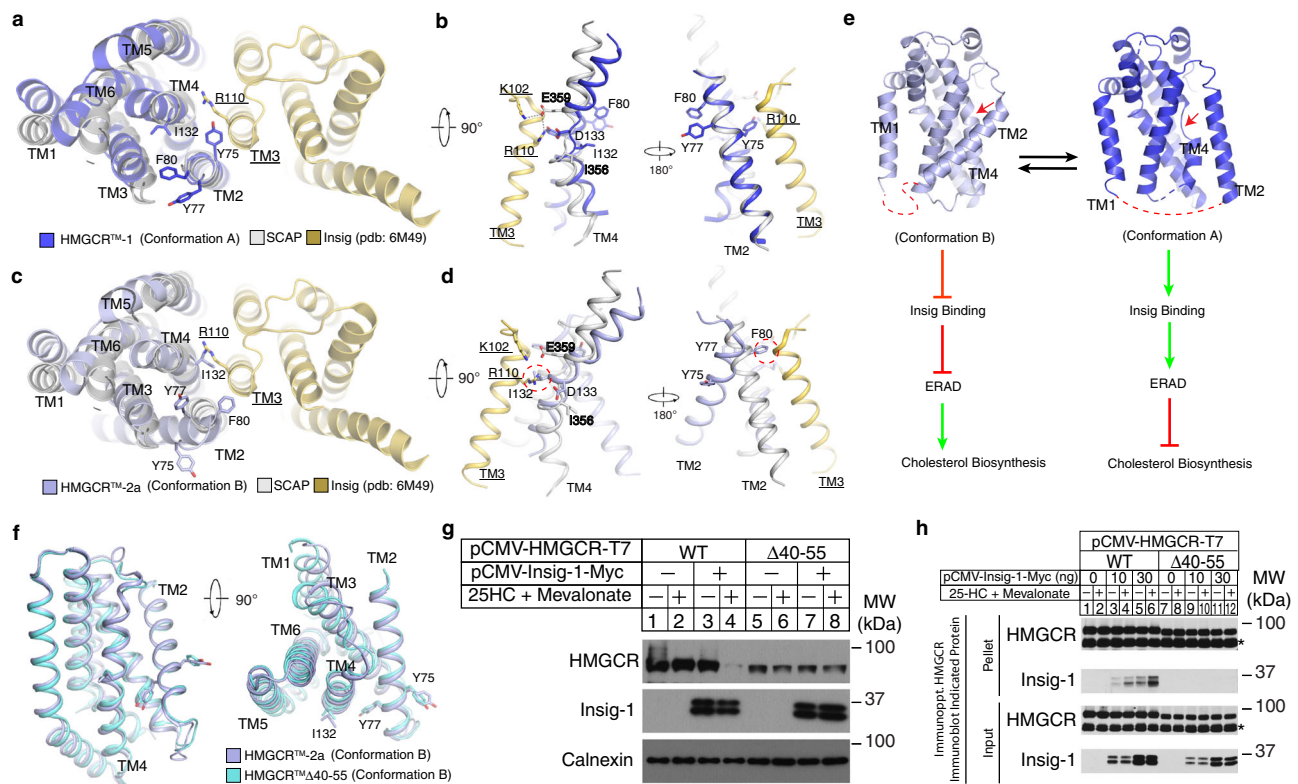


**Fig. 5 | The structural comparison of HMGCR to Insig-bound Scap reveals dynamic features of the SSD. a** HMGCR-TMs 1–6 (Conformation A) docked to the structure of the Scap-Insig complex. The residue Y75 and Y77 of YIYF motif is shown in sticks. **b** HMGCR-TMs 1–6 (Conformation A) docked to the structure of SCAP-Insig complex. The TMs of Insig are indicated by underlining. Interactions between amino acids in Scap and Insig are indicated by dashed lines. **c** HMGCR-TMs 1–6 (Conformation B) docked to the structure of the Scap-Insig complex. **d** HMGCR-TMs 1–6 (Conformation B) docked to the structure of SCAP-Insig complex. The conformation of TM2 when HMGCR adopts Conformation B interferes with the putative interaction between HMGCR and Insig. The clashes between Insig R110 and HMGCR-I132; Insig-TM3 and HMGCR-F80 are indicated by dashed circles. **e** L1–2 regulates the conformational transition of HMGCR-SSD. L1–2 is indicated by the red dashed lines. **f** Structural comparison of HMGCR<sup>TM</sup>-2a and HMGCR<sup>TM</sup> (Δ40–55).

**g** HMGCR-deficient Chinese hamster ovary (CHO) cells transfected with expression plasmids encoding indicated variant of HMGCR-T7 and Insig-1-Myc were treated in the absence or presence of 1 μg/ml 25-HC and 10 mM mevalonate and were then harvested and lysed. Aliquots of whole cell lysates were subjected to SDS-PAGE, followed by immunoblot analysis with IgG-A9 (against HMGR) or anti-Myc (IgG-9E10, against Insig-1). **h** HMGCR-deficient CHO cells transfected with expression plasmids encoding the indicated HMGR variant and Insig-1 were depleted of sterols for 16 h. The cells were then pretreated with the proteasome inhibitor MG-132 for 1 h, followed by treatment with 1 μg/ml 25-HC for 30 min. Cells were then harvested, lysed, and subjected to immunoprecipitation followed by immunoblot analysis with anti-T7 (against HMGR) or anti-Myc (IgG-9E10, against Insig-1). Asterisks indicate nonspecific bands. Additional experimental details can be found in “Methods”. Source data are provided as a Source Data file.

analysis of the resolved structure revealed that HMGCR<sup>TM</sup> adopts two distinct conformations designated Conformation A and Conformation B (Fig. 4a, b). In UBIAD1-HMGCR complex 1 and 2b, HMGCR<sup>TM</sup> assumes Conformation A in which TM2 is perpendicular to the membrane, whereas TM4 is unwound to generate two half helices that we designate TM4a and TM4b (Fig. 4b). HMGCR<sup>TM</sup> assumes Conformation B in UBIAD1-HMGCR complex 2a. TM2 is tilted 45° in the membrane (Fig. 4a) and TM4 forms an intact α-helix (Fig. 4b). In the dimeric state of complex 2a, Conformation B becomes stabilized through direct interactions between TMs of HMGR.

SSDs are found in five other proteins—Scap, Niemann-Pick C1 (NPC1), NPC1-Like1 (NPC1L1), Patched, and Dispatched—implicated in the regulation of cholesterol metabolism and signaling (Supplementary Fig. 10). Scap is a cholesterol-regulated escort protein required for activation of membrane-bound transcription factors called sterol regulatory element-binding proteins (SREBPs)<sup>40</sup>. NPC1 and NPC1L1 mediate intracellular transport of LDL-derived or dietary cholesterol<sup>41</sup>. Patched binds to the cholesterol-modified morphogen Hedgehog, while Dispatched mediates release of Hedgehog from cells<sup>42</sup>. Scap and HMGR are unique among SSD-containing proteins in that sterols cause both proteins to bind Insigs. However, Insig binding does not lead to accelerated ERAD of Scap. Instead, the reaction traps Scap in

the ER, preventing its transport to the Golgi for proteolytic activation of bound SREBPs<sup>43</sup>.

The structures of NPC1, NPC1L1, Patched, Dispatched, and Scap in complex with Insig-2, have been determined<sup>44–53</sup>. TMs 2–6 constitute the SSD in HMGR, Scap, and Patched, whereas TMs 3–7 constitutes the NPC1-SSD and NPC1L1-SSD. The TMs of NPC1, NPC1L1, Patched, and Dispatched contain at least 12 transmembrane helices including a pseudo-SSD that associates with the SSD to restrain its conformation (Supplementary Fig. 11). We compared the structures of HMGR (TMs 1–6), Scap (TMs 1–6), NPC1 (TMs 2–7) and Patched (TMs 1–6). These comparisons revealed the structure of HMGR (TMs 1–6) in Conformation A is similar to that of Insig-bound Scap (Fig. 4c). TM2 in both SSDs is vertical in the membrane and remarkably, TM4 is broken at similar positions (Fig. 4c, Supplementary Fig. 10). The tilted conformation of HMGR-TM2 is not observed in corresponding TMs of NPC1 (TM3) and Patched (TM2). NPC1-TM5 and Patched-TM4 correspond to HMGR-TM4 and resemble its configuration when HMGR<sup>TM</sup> assumes Conformation B (Fig. 4d, e).

### Dynamic Reorganization of TMs in the HMGR SSD

Further analysis of the two HMGR SSD conformations may provide insight into mechanisms for the sterol-sensing reaction. Thus, we superimposed the structure of TMs 1–6 of HMGR in Conformation A

with the previously reported structure of the Scap-Insig-2 complex<sup>50</sup>. This superimposition indicates that the predicted HMGCR-Insig-2 interface is similar to the Scap-Insig interface, which is comprised of TMs 2, 4, and 5 of Scap and TMs 3 and 4 of Insig-2 (Fig. 5a). A previous finding suggested that unwinding of Scap-TM4 exposes negatively charged E359, permitting interaction with R110 (and perhaps K102) of Insig-2 that stabilizes the Scap-Insig-2 complex<sup>50</sup>. Our modeling predicts that D133 of HMGCR assumes a position equivalent to that of E359 in the broken TM4 of Scap and contributes to formation of the HMGCR-Insig-2 complex (Fig. 5b). The YIYF motif of Scap and HMGCR, which is required for their sterol-induced binding to Insigs<sup>50</sup>, is positioned similarly in TM2 of both proteins (Fig. 5b).

Figure 5c shows the superimposed structures of the Scap-Insig-2 complex and HMGCR (TMs 1–6) in Conformation B that results in rotation of TM2 and TM4 approximately 180° (Fig. 5a, c). This rotation causes significant steric hindrance between F80 and Insig-2-TM3; steric clash is also observed between I132 in HMGCR and R110 of Insig-2 (Fig. 5c, d). It is notable that in the absence of Insig-2, Scap-TM2 is not observed in the cryo-EM maps, which indicates considerable flexibility. TM4 is not broken and may adopt a continuous  $\alpha$ -helix similar to that of HMGCR-TM4 in Conformation B (Supplementary Fig. 12)<sup>49</sup>.

Comparing the structure of HMGCR to that of Scap and other SSD-containing proteins led us to speculate that when HMGCR adopts Conformation B, the SSD cannot bind to Insigs and resists ERAD. However, adoption of Conformation A promotes binding of HMGCR to Insig for subsequent ubiquitination and ERAD. Analysis of the HMGCR structure led us to postulate that flexibility of the luminal loop between TM1 and TM2 (L1–2) may affect the conformation of TM2, leading to reorganization of TMs within the SSD that regulates HMGCR ERAD (Fig. 5e). Thus, we screened several variants of HMGCR harboring deletions within L1–2 that reduce flexibility and restrict the conformation of the SSD. We identified one variant, designated HMGCR<sup>TM</sup> ( $\Delta$ 40–55), harboring a 16-amino acid deletion that exhibits reasonable expression yield and sufficient biochemical behavior. Cryo-EM analysis of the HMGCR<sup>TM</sup> ( $\Delta$ 40–55)-UBIAD1<sup>N102S</sup> complex revealed that the L1–2 deletion caused HMGCR to exclusively assume Conformation B in which TM2 is tilted in the membrane; TM4 is intact regardless of its monomeric and dimeric state (Fig. 5f, Supplementary Figs. 3f, 13). To validate these structural observations, we examined the sterol-accelerated ERAD of T7-tagged HMGCR harboring the L1–2 deletion (designated HMGCR-T7 ( $\Delta$ 40–55)). HMGCR-T7 (WT) was subjected to Insig-mediated ERAD stimulated by the oxysterol 25-hydroxycholesterol (25-HC) and mevalonate (which provides a source of GGpp) (Fig. 5g, lanes 1–4). In contrast, HMGCR-T7 ( $\Delta$ 40–55) completely resisted 25-HC-induced ERAD (Fig. 5g, lanes 5–8). Co-immunoprecipitation was used to measure sterol-mediated association of HMGCR-T7 (WT) and ( $\Delta$ 40–55) with Insig-1. The results show that 25-HC enhanced the co-precipitation of Insig-1 with HMGCR-T7 (WT) (Fig. 5h, lanes 1–6), but not HMGCR-T7 ( $\Delta$ 40–55) (Fig. 5h, lanes 7–12). Based on these findings, we conclude that flexibility of L1–2 significantly contributes to reorganization of the SSD that permits binding of Insigs.

## Discussion

Previous studies have described an intricate pathway through which distinct lipids—sterols and GGpp—accelerate Insig-mediated ERAD of HMGCR<sup>3</sup>. A key breakthrough in the understanding of HMGCR ERAD came with the discovery that UBIAD1 binds to HMGCR and inhibits its ERAD. In the current studies, we analyze the structure of the HMGCR-UBIAD1 complex, which reveals a hydrophobic interface that is mediated by multiple interactions between the TMs of UBIAD1 and HMGCR (Fig. 1c–g). Mutation of key residues in this interface disrupts formation of the HMGCR-UBIAD1 complex and blunts UBIAD1-mediated stabilization of HMGCR (Fig. 2d–f). Identification of the HMGCR-UBIAD1 interface has

important implications for the molecular basis of statin-induced accumulation of HMGCR that was described more than 40 years ago<sup>2</sup>. Studies in genetically-manipulated mice revealed that inhibition of ERAD substantially contributes to statin-accumulation of HMGCR<sup>16</sup>. UBIAD1 is sequestered in the ER of hepatic membranes isolated from statin-fed mice owing to depletion of GGpp<sup>25</sup> and unequivocal genetic evidence has been obtained that UBIAD1 is an inhibitor of HMGCR ERAD<sup>36</sup>. Taken together with the current study, we predict molecules that disrupt the HMGCR-UBIAD1 interface or mimic GGpp in stimulating ER-to-Golgi translocation of UBIAD1 will enhance ERAD of HMGCR, preventing its accumulation associated with statin therapy.

We captured the SSD of HMGCR in two distinct conformations, indicating TMs in the region undergo dynamic reorganization within ER membranes (Fig. 5e). Importantly, the cytosolically-exposed sites for sterol-induced ubiquitination (K89 and K248) are identical in both conformations, ruling out the possibility that reorganization of the SSD alters access of the sites to ubiquitination machinery. We attenuated the structural rearrangement of TMs in the SSD through protein engineering and discovered that confining HMGCR to Conformation B (Fig. 5f) abolished its Insig-mediated ERAD stimulated by 25-HC (Fig. 5g). Certain oxysterols such as 25-HC are known to bind Insigs and it has been postulated that oxysterol-bound Insig in turn, associates with the SSDs of Scap and HMGCR<sup>40</sup>. Taking our current study into consideration, it is reasonable to speculate that oxysterol-bound Insig only engages the SSD when it assumes Conformation A. It should be also noted that the cholesterol synthesis intermediate 24,25-dihydroxysterol (DHL) accelerates Insig-mediated ERAD of HMGCR<sup>3</sup>, but does not bind to Scap or Insig. We hypothesize that the SSD of HMGCR directly senses the concentration of DHL embedded in ER membranes, causing the protein to change its conformation to engage Insigs for ubiquitination and ERAD to control the synthesis of cholesterol. Although the structures of other SSD-containing proteins have been determined<sup>44–53</sup>, these studies neither observed the dynamic reorganization of the SSD nor determined whether multiple conformations of the SSD modulated the protein's activity. Our findings provide structural evidence validated by functional assays that are beginning to disclose the molecular basis through which SSDs control protein function.

Despite the advance in the understanding of the HMGCR ERAD pathway, several questions remain outstanding. For example, molecular mechanisms underlying transition of the HMGCR-SSD between Conformations A and B regulated by DHL and oxysterols remain to be determined. The precise mechanism through which UBIAD1 inhibits HMGCR ERAD at a post-ubiquitination step in the reaction has not been elucidated. Finally, mechanisms whereby GGpp dissociates the HMGCR-UBIAD1 complex and stimulates ER-to-Golgi transport of UBIAD1 is unknown. Attempts to address these important questions utilizing a variety of approaches are currently underway.

## Methods

### Expression plasmids

A cDNA encoding the transmembrane domain (amino acids 1–356) of hamster HMGCR harboring mutations (K89R, K248R) that abolish the enzyme's sterol-induced ubiquitination was cloned into the pEZT-BM vector<sup>54</sup> with a N-terminal FLAG tag. The resulting expression plasmid is designated pEZT-BM-FLAG-HMGCR<sup>TM</sup>. The cDNA for hamster UBIAD1 containing a 40-amino acid deletion at N-terminus and the SCD-associated N102S mutation was cloned into pEZT-BM vector preceded by a StrepII tag. BRIL insertion was screened through different replacement for loops between TMs of UBIAD1. The final construct used for cryo-EM structure determination is the one with BRIL insertion located between Phe300 and Pro309. This expression

plasmid is designated pEZT-BM-StrepII-UBIADI-BRIL<sup>N102S</sup>. The following expression plasmids were described in the indicated reference: pCMV-HMGCR (TM1-8)-T7 encoding amino acids 1–346 of hamster HMGCR with 3 copies of the T7 epitope at the C-terminus under transcriptional control of the cytomegalovirus (CMV) promoter<sup>8</sup>; pCMV-Myc-UBIADI (N102S) encoding human UBIADI containing a Myc tag at the N-terminus under control of the CMV promoter<sup>17</sup>; pCMV-Insig-1-Myc, which encodes human Insig followed by six copies of the Myc epitope under control of the CMV promoter<sup>43</sup>; and pCMV-HMGCR-7, encoding full-length hamster HMGCR followed by three copies of the T7 epitope under control of the CMV promoter<sup>9</sup>. Site-directed mutagenesis of pCMV-HMGCR (TM1-8)-T7, pEZT-BM-FLAG-HMGCR<sup>TM</sup>, and pEZT-BM-StrepII-UBIADI<sup>N102S</sup> (without BRIL insertion) was carried out by two-step overlapping PCR. All mutations were verified by sequencing.

### Cloning, expression, and purification of HMGCR<sup>TM</sup>-UBIADI<sup>N102S</sup> complex

pEZT-BM-FLAG-HMGCR<sup>TM</sup> and pEZT-BM-StrepII-UBIADI-BRIL<sup>N102S</sup> were introduced into HEK-293S GnT<sup>-</sup> cells (ATCC) by baculovirus-mediated transduction. Following incubation for 60 h at 30 °C, cells were harvested and disrupted by sonication in buffer A (20 mM HEPES pH 7.5, 150 mM NaCl) containing 1 mM PMSF, 10 µg/ml leupeptin. After low-speed centrifugation, the resulting supernatant was incubated with 1% (w/v) lauryl maltose neopentyl glycol (LMNG, Anatrace), 0.1% cholesteryl hemisuccinate (CHS, Steraloids) at 4 °C for 1 h. Lysates were clarified by centrifugation at 20,000 × g; the supernatant of this spin was loaded onto an anti-FLAG M2 affinity column (Sigma). After washing twice with buffer B (20 mM HEPES pH 7.5, 400 mM NaCl, 0.1% LMNG, 0.01% CHS, 10 µg/ml POPS and 10 µg/ml Soybean Polar Lipid Extract), bound proteins were eluted in buffer C (20 mM HEPES pH 7.5, 150 mM NaCl, 0.1% LMNG, 0.01% CHS, 10 µg/ml POPS, 10 µg/ml Soybean Polar Lipid Extract and 0.1 mg/ml FLAG peptide). The sample was concentrated and further purified by Superose-6 size-exclusion chromatography (GE Healthcare) in buffer D (20 mM HEPES pH 7.5, 150 mM NaCl and 0.06% Digitonin). The peak fractions were collected for complex assembly. The HMGCR<sup>TM</sup> (Δ40–55)-UBIADI-BRIL<sup>N102S</sup> complex was expressed and purified using the identical procedure.

### Expression and purification of anti-BRIL Fab and its nanobody

The anti-BRIL Fab (Fab<sup>BRIL</sup>) was expressed in *E. coli* and purified as described<sup>34</sup>. The DNA sequence encoding the anti-Fab<sup>BRIL</sup> nanobody (Nb) was derived from PDB: 6WW2<sup>55</sup> and synthesized from Integrated DNA Technologies and cloned into pET-26b vector with a C-terminal 6×His tag. The nanobody was expressed in *E. coli* BL21-Gold (DE3) cells with 0.5 mM IPTG at 25 °C overnight and purified by Ni-NTA chromatography and size-exclusion chromatography on a Superdex 200 column. The proteins were concentrated and frozen at –80 °C for further use.

### Generation of Fab<sup>15B2</sup>

Monoclonal antibody (designated 15B2) of isotype IgG1 were raised in mice (NZBWF1/J, The Jackson Laboratory) at the Department of Molecular Genetics of the University of Texas Southwestern Medical Center. The antigen immunize mice was the HMGCR<sup>TM</sup>-UBIADI<sup>N102S</sup> complex that was reconstituted into Amphipol A8-35. Hybridomas were created by fusion of splenic B lymphocytes from hyperimmune mice to SP2-mIL6 mouse myeloma cells (ATCC, CRL-2016). We used the combined techniques of ELISA, immunoblot analysis, and immunoprecipitation to identify antibodies that preferentially bound to HMGCR<sup>TM</sup>-UBIADI<sup>N102S</sup> complex in its native, but not SDS-denatured state. These efforts yielded a mouse monoclonal antibody designated IgG-15B2. To clone IgG-15B2, total RNA was isolated from the hybridoma by RNA extraction kit (Qiagen) following the manufacturer's protocol. Total RNA was subjected to reverse transcription reactions

using Superscript III reverse transcription kit (Invitrogen) and the resultant cDNA was used as a template in PCR reactions with degenerate primers to amplify the variable regions. Sequences of the resulting PCR products were analyzed with the IMGT database (<http://www.imgt.org/>) to determine the variable regions of the light chain and heavy chain, which were then cloned into shuttle vectors for light chain and the Fab region of heavy chain with a C-terminal 6×His tag, respectively<sup>56</sup>. The resulting constructs were co-transfected to HEK-293S GnT<sup>-</sup> cells (ATCC) for expression at 37 °C. After 72 h, the medium was harvest and applied to Ni-NTA gravity columns. Following several washes with buffer A containing 20 mM imidazole, bound material was eluted with buffer A containing 250 mM imidazole. The eluate was then applied to a Superdex-200 Increase size-exclusion chromatography column (GE Healthcare) in buffer A and peak fractions containing Fab<sup>15B2</sup> were collected for complex assembly.

### Cryo-EM sample preparation

To assemble the HMGCR<sup>TM</sup>-UBIADI-BRIL<sup>N102S</sup>-Fab<sup>BRIL</sup>-Nb complex, purified HMGCR<sup>TM</sup>-UBIADI-BRIL<sup>N102S</sup> was first incubated with Amphipol A8-35 (Anatrace) for 4 h at 4 °C. The detergent was then removed by overnight incubation with Bio-beads (Bio-Rad). The amphipol-solubilized complex was mixed with Fab<sup>BRIL</sup> and Nb at 1:1.5:2.25 molar ratio for 1 hour at 4 °C. The HMGCR<sup>TM</sup>-UBIADI-BRIL<sup>N102S</sup>-Fab<sup>BRIL</sup>-Nb complex was finally purified with a Superose-6 column (GE Healthcare) in buffer A. Peak fractions containing the assembled complex were concentrated to –10 mg/ml and 2 mM Fluorinated Fos-Choline-8 (Anatrace) was added to the sample before making grids. To assemble the HMGCR<sup>TM</sup>-UBIADI-BRIL<sup>N102S</sup>-Fab<sup>15B2</sup> complex, purified HMGCR<sup>TM</sup>-UBIADI-BRIL<sup>N102S</sup> and Fab<sup>15B2</sup> were mixed at 1:1.1 molar ratio and incubated on ice for 1 h, followed by gel-filtration with a Superose-6 column (GE Healthcare) in buffer D. Peak fractions that contained the HMGCR<sup>TM</sup>-UBIADI-BRIL<sup>N102S</sup>-Fab<sup>15B2</sup> complex were concentrated to –10 mg/ml. Preparation of HMGCR<sup>TM</sup> (Δ40–55)-UBIADI-BRIL<sup>N102S</sup>-Fab<sup>15B2</sup> complex sample was following the same procedure.

### Cryo-EM imaging and data processing

The freshly purified complexes samples were added to Glow discharged Quantifoil R1.2/1.3 400 mesh Au holey carbon grids (Quantifoil), blotted using a Vitrobot Mark IV (FEI), and frozen in liquid ethane. The grids were imaged in a 300 kV Titan Krios (FEI) with a Gatan K3 Summit direct electron detector (Gatan). Data were collected using SerialEM<sup>57</sup> at 0.83 Å/pixel or 0.842 Å/pixel. Images were recorded for 5-second exposures in 50 subframes with a total dose of ~60 electrons per Å<sup>2</sup>. Data were collected in super-resolution mode and the parameters of data collection are summarized in the Supplementary Table 1.

For all the three samples, Dark subtracted movie stacks were normalized by gain reference and the motion correction was performed using MotionCor2<sup>58</sup>. The contrast transfer function (CTF) was estimated using CTFIND4<sup>59</sup>. After particle picking by crYOLO<sup>60</sup>, the low-quality images and false-positive particles were removed manually. For the HMGCR<sup>TM</sup>-UBIADI-BRIL<sup>N102S</sup>-Fab<sup>BRIL</sup>-Nb complex, three data sets were collected. After 2D-classification of data set 1 in CryoSPARC<sup>61</sup>, classes with clean background were selected to generate initial models for the 3D-classification. Map from the best 3D class showing clear features of micelle, Fab and Nb were used as a model to fish out “good” particles from all the three data sets via 3D-classification. The resulting particles were subjected to the secondary 3D-classification with a mask in RELION-3<sup>62</sup>. Particles from the good classes were polished and 3D classified in RELION-3. The best class was selected for the final 3D-refinement in RELION-3. For HMGCR<sup>TM</sup>-UBIADI-BRIL<sup>N102S</sup>-Fab<sup>15B2</sup> complexes, good classes from the initial 2D-classification were select to generated initial models for the 3D-classification of the entire particle set in CryoSPARC. The best 3D class was 2D classified and the classes showing features of monomer or



dimer were selected separately to refine the best 3D model, respectively. The resulting maps were used as models for the further 3D-classification. 3D classes containing monomeric or dimeric particles were subjected to 2D-classification in CryoSPARC to remove the heterogeneous particles. The remaining particles in the two classes were polished in RELION-3, followed by CTF refinement and final 3D refinement in CryoSPARC, respectively. For HMGCRTM ( $\Delta 40-55$ )-UBIAD1-BRIL<sup>N102S</sup>-Fab<sup>15B2</sup> complexes, monomeric and dimeric maps from HMGCRTM-UBIAD1-BRIL<sup>N102S</sup>-Fab<sup>15B2</sup> complexes were used as models for 3D-classification in CryoSPARC. Particles from the monomeric and dimeric classes were applied to 2D-classification and a secondary 3D-classification to further exclude the bad particles. The remaining particles in the two classes were CTF refined follow by the final local 3D refinement in CryoSPARC, respectively.

### Model Construction, Refinement and Validation

For the HMGCRTM-UBIAD1-BRIL<sup>N102S</sup>-Fab<sup>15B2</sup> complex, a HMGCRTM-UBIAD1-BRIL<sup>N102S</sup> structure predicted by AlphaFold<sup>63</sup> and a Fab<sup>15B2</sup> structure predicted by Swiss-Model<sup>64</sup> were docked into the Complex-1 map as the initial model. The refined Complex-1 structure was docked into the Complex-2a region of the Complex-2 map used as the initial model for Complex-2a. Both structure models were manually built by COOT<sup>65</sup>, followed by refinement in real space using PHENIX<sup>66</sup> and in reciprocal space using Refmac with secondary-structure restraints and stereochemical restraints<sup>67</sup>. For cross-validation, the final model was refined with the half map 1 from the final 3D-refinement. The resulting model was used to calculate the model vs. map FSC curve against half map 1 and 2, respectively, using the Comprehensive validation module in PHENIX. MolProbity<sup>68</sup> was used to validate the geometries of the model. Structure figures were generated using PyMOL (<http://www.pymol.org>), Chimera<sup>69</sup> and ChimeraX<sup>70</sup>. The Complex-1 structure with the deletion of TMs 7-8 of UBIAD1 was docked into the Complex-2b region of the Complex-2 map as the initial model for Complex-2b. The Complex-2b structure was refined once in real space using PHENIX for figures. For the HMGCRTM-UBIAD1-BRIL<sup>N102S</sup>-Fab<sup>BRIL</sup>-Nb complex, HMGCRTM-UBIAD1-BRIL<sup>N102S</sup> structure from Complex-1 and Fab<sup>BRIL</sup>-Nb structure from PDB: 6WW2 were docked into map as the initial model. The structure model was manually built by COOT and refined once in real space using PHENIX for figure preparation. For HMGCRTM ( $\Delta 40-55$ )-UBIAD1-BRIL<sup>N102S</sup>-Fab<sup>15B2</sup> complexes, structure of HMGCRTM-UBIAD1-BRIL<sup>N102S</sup>-Fab<sup>15B2</sup> Complex-2a was docked into the monomeric and dimeric maps, respectively, as initial models. The structure models were manually built by COOT and refined once in real space using PHENIX for figure preparation.

### Transient Transfection and Immunoprecipitation

HEK-293S GnT1<sup>-</sup> cells were maintained in suspension in FreeStyle 293 expression medium (Gibco, Cat# 12338-026) containing 2% FCS, 100 units/ml penicillin and 100 mg/ml streptomycin sulfate at 37 °C, 8% CO<sub>2</sub>. Cells were set up for experiments on day 0 at the density of  $0.6 \times 10^6$  cells per 60-mm dish. On day 1, cells were transfected with variants of pEZT-BM-FLAG-HMGCRTM, and pEZT-BM-StrepII-UBIAD1<sup>N102S</sup> ( $\Delta 1-40$ , without BRIL insertion) indicated in Figure Legends using the FuGENE 6 transfection reagent (Promega, Cat# E2692), as described in ref. 8. On day 3, duplicate dishes of cells were harvested and washed with PBS. The resulting cell pellets were resuspended in buffer containing 20 mM HEPES, pH7.5, 150 mM NaCl, 0.4% sodium cholate, 0.4% DDM, 0.2% LMNG, 0.02% CHS, and protease inhibitor cocktail (Roche, Cat# 04693124001). The cell suspension was lysed by rotating for 1 hour at 4 °C followed by centrifugation at  $20,000 \times g$  for 15 min at 4 °C to obtain the cell lysates. Aliquots of the supernatant were added to anti-FLAG M2 affinity agarose gel (MilliporeSigma, Cat# A2220) and incubated for 2 hours at 4 °C. Aliquots of lysates and elution fractions from immunoprecipitations were subjected to SDS-PAGE and immunoblot analysis. Primary antibodies used

for immunoblotting analysis included: mouse monoclonal anti-FLAG tag IgG-FLA-1 (MBL International, Cat# M185-3L, 1:3000 dilution), mouse monoclonal anti-StrepII tag IgG-5A9F9 (GenScript, Cat# A01732, 1:3000 dilution), and mouse monoclonal anti- $\beta$ -Tubulin IgG-D3U1W (Cell Signaling Technology, Cat# 86298 S, 1:3000 dilution).

SV-589 ( $\Delta$ UBIAD1) cells (Fig. 2e, f) were maintained as described previously<sup>21</sup> and set up for experiments on day 0 at  $4 \times 10^5$  cells per 60-mm dish. On day 1, cells were transfected with variants of pCMV-HMGCRTM (TMI-8)-T7, Myc-UBIAD1 (N102S), and pEZT-BM-StrepII-UBIAD1<sup>N102S</sup> (without BRIL insertion) (0.5  $\mu$ g/dish) as indicated in the Figure Legends using X-tremeGENE<sup>TM</sup> HP transfection reagent (Roche) (3  $\mu$ l/ $\mu$ g DNA). On day 3, cells were harvested, lysed, and subjected to subcellular fractionation as described<sup>8</sup>. HMGCRTM-deficient UT-2 cells (Fig. 5g, h) were maintained as described previously<sup>71</sup> and set up for experiments on day 0 at  $5 \times 10^5$  cells per 60-mm dish. On day 1, the cells were transfected with pCMV-HMGCRTM-T7 (WT) or ( $\Delta 40-55$ ) (1  $\mu$ g/dish) in the absence or presence of 10–30 ng of pCMV-Insig-1-Myc using X-tremeGENE<sup>TM</sup>-360 transfection reagent (Roche) (3  $\mu$ l/ $\mu$ g DNA). The cells were depleted of sterol and nonsterol isoprenoids through incubation in medium supplemented with lipoprotein-deficient serum, 10  $\mu$ M of the statin compactin, and 50  $\mu$ M sodium mevalonate.

After 24 h at 37 °C, cells were harvested and subjected to subcellular fractionation as described above. Aliquots of membrane fractions isolated from transfected SV-589 ( $\Delta$ UBIAD1) (Fig. 2e, f) and whole cell lysates of transfected UT-2 cells (Fig. 5g) were subjected to SDS-PAGE and immunoblot analysis was carried out with anti-T7 Tag antibody (MilliporeSigma, Cat# 69522, 1:5000 dilution), IgG-A9 a mouse monoclonal antibody against endogenous HMGCRTM (clone IgG-A9, MilliporeSigma, Cat# MABS1233, 1:1000 dilution), IgG-9E10 against the Myc epitope (MilliporeSigma, Cat# M4439, 1:5000 dilution), mouse monoclonal anti-StrepII Tag IgG, and anti-calnexin polyclonal antibody (Novus Biologicals, Cat# NB100-1965, 1:1000 dilution). For the immunoprecipitation experiment shown in Fig. 5h, transfected UT-2 cells were harvested, lysed in PBS containing 1% digitonin, and immunoprecipitated with anti-T7-coupled beads (MilliporeSigma, Cat# 69026). Aliquots of lysates and pellets of the immunoprecipitation were subjected to SDS-PAGE and immunoblot analysis with anti-T7 and IgG-9E10. Uncropped blots can be found in the Source Data file.

### Statistics and reproducibility

The experiments in Figs. 2d–f, 5g, h and Supplementary Figs. 2, 3a–c were repeated at least two times on different days. Similar results were obtained.

### Reporting summary

Further information on research design is available in the Nature Research Reporting Summary linked to this article.

### Data availability

Data supporting the findings of this manuscript are available from the corresponding author upon reasonable request. The 3D cryo-EM density maps have been deposited in the Electron Microscopy Data Bank under the accession numbers EMD-27461 (complex in state 1), EMD-27460 (complex in state 2), EMD-27475 (complex in amphipols), EMD-27478 (Complex  $\Delta 40-55$  in state 1), and EMD-27477 (Complex  $\Delta 40-55$  in state 2). Atomic coordinates for the models have been deposited in the Protein Data Bank under the accession numbers 8DJM [<https://doi.org/10.2210/pdb8DJM/pdb>] (complex in state 1) and 8DJK [<https://doi.org/10.2210/pdb8DJK/pdb>] (complex in state 2). Source Data underlying Figs. 2d–f and 5g, h are provided as a Source Data file. Source data are provided with this paper.

### References

- Goldstein, J. L. & Brown, M. S. Regulation of the mevalonate pathway. *Nature* **343**, 425–430 (1990).

2. Brown, M. S. & Goldstein, J. L. Multivalent feedback regulation of HMG CoA reductase, a control mechanism coordinating isoprenoid synthesis and cell growth. *J. Lipid Res.* **21**, 505–517 (1980).
3. Schumacher, M. M. & DeBose-Boyd, R. A. Posttranslational regulation of HMG CoA reductase, the rate-limiting enzyme in synthesis of cholesterol. *Annu. Rev. Biochem.* **90**, 659–679 (2021).
4. Luo, J., Yang, H. & Song, B. L. Mechanisms and regulation of cholesterol homeostasis. *Nature Rev. Molecular Cell Biol.* <https://doi.org/10.1038/s41580-019-0190-7> (2019).
5. Sharpe, L. J., Coates, H. W. & Brown, A. J. Post-translational control of the long and winding road to cholesterol. *J. Biol. Chem.* **295**, 17549–17559 (2020).
6. Nakanishi, M., Goldstein, J. L. & Brown, M. S. Multivalent control of 3-hydroxy-3-methylglutaryl coenzyme A reductase. Mevalonate-derived product inhibits translation of mRNA and accelerates degradation of enzyme. *J. Biol. Chem.* **263**, 8929–8937 (1988).
7. Ravid, T., Doolman, R., Avner, R., Harats, D. & Roitelman, J. The ubiquitin-proteasome pathway mediates the regulated degradation of mammalian 3-hydroxy-3-methylglutaryl-coenzyme A reductase. *J. Biol. Chem.* **275**, 35840–35847 (2000).
8. Sever, N., Yang, T., Brown, M. S., Goldstein, J. L. & DeBose-Boyd, R. A. Accelerated degradation of HMG CoA reductase mediated by binding of insig-1 to its sterol-sensing domain. *Mol. Cell* **11**, 25–33 (2003).
9. Sever, N. et al. Insig-dependent ubiquitination and degradation of mammalian 3-hydroxy-3-methylglutaryl-CoA reductase stimulated by sterols and geranylgeraniol. *J. Biol. Chem.* **278**, 52479–52490 (2003).
10. Skalnik, D. G., Narita, H., Kent, C. & Simoni, R. D. The membrane domain of 3-hydroxy-3-methylglutaryl-coenzyme A reductase confers endoplasmic reticulum localization and sterol-regulated degradation onto beta-galactosidase. *J. Biol. Chem.* **263**, 6836–6841 (1988).
11. Roitelman, J., Olender, E. H., Bar-Nun, S., Dunn, W. A. Jr. & Simoni, R. D. Immunological evidence for eight spans in the membrane domain of 3-hydroxy-3-methylglutaryl coenzyme A reductase: implications for enzyme degradation in the endoplasmic reticulum. *J. Cell Biol.* **117**, 959–973 (1992).
12. Jo, Y., Lee, P. C., Sguigna, P. V. & DeBose-Boyd, R. A. Sterol-induced degradation of HMG CoA reductase depends on interplay of two Insigs and two ubiquitin ligases, gp78 and Trc8. *Proc. Natl. Acad. Sci. USA* **108**, 20503–20508 (2011).
13. Song, B. L., Sever, N. & DeBose-Boyd, R. A. Gp78, a membrane-anchored ubiquitin ligase, associates with Insig-1 and couples sterol-regulated ubiquitination to degradation of HMG CoA reductase. *Mol. cell* **19**, 829–840 (2005).
14. Jiang, L. Y. et al. Ring finger protein 145 (RNF145) is a ubiquitin ligase for sterol-induced degradation of HMG-CoA reductase. *J. Biol. Chem.* **293**, 4047–4055 (2018).
15. Morris, L. L., Hartman, I. Z., Jun, D. J., Seemann, J. & DeBose-Boyd, R. A. Sequential actions of the AAA-ATPase Valosin-containing Protein (VCP)/p97 and the Proteasome 19 S regulatory particle in sterol-accelerated, endoplasmic reticulum (ER)-associated degradation of 3-Hydroxy-3-methylglutaryl-coenzyme A reductase. *J. Biol. Chem.* **289**, 19053–19066 (2014).
16. Hwang, S. et al. Contribution of accelerated degradation to feedback regulation of 3-Hydroxy-3-methylglutaryl coenzyme A reductase and cholesterol metabolism in the liver. *J. Biol. Chem.* **291**, 13479–13494 (2016).
17. Schumacher, M. M., Elsabrouty, R., Seemann, J., Jo, Y. & DeBose-Boyd, R. A. The prenyltransferase UBIAD1 is the target of geranylgeraniol in degradation of HMG CoA reductase. *eLife* **4**, <https://doi.org/10.7554/eLife.05560> (2015).
18. Jiang, S. Y. et al. Schnyder corneal dystrophy-associated UBIAD1 mutations cause corneal cholesterol accumulation by stabilizing HMG-CoA reductase. *PLoS Genet.* **15**, e1008289 (2019).
19. Nakagawa, K. et al. Identification of UBIAD1 as a novel human menaquinone-4 biosynthetic enzyme. *Nature* **468**, 117–121 (2010).
20. Hirota, Y. et al. Functional characterization of the vitamin K2 biosynthetic enzyme UBIAD1. *PLoS ONE* **10**, e0125737 (2015).
21. Schumacher, M. M., Jun, D. J., Johnson, B. M. & DeBose-Boyd, R. A. UbiA prenyltransferase domain-containing protein-1 modulates HMG-CoA reductase degradation to coordinate synthesis of sterol and nonsterol isoprenoids. *J. Biol. Chem.* **293**, 312–323 (2018).
22. Schumacher, M. M., Jun, D. J., Jo, Y., Seemann, J. & DeBose-Boyd, R. A. Geranylgeranyl-regulated transport of the prenyltransferase UBIAD1 between membranes of the ER and Golgi. *J. Lipid Res.* **57**, 1286–1299 (2016).
23. Orr, A. et al. Mutations in the UBIAD1 gene, encoding a potential prenyltransferase, are causal for Schnyder crystalline corneal dystrophy. *PLoS ONE* **2**, e685 (2007).
24. Weiss, J. S. et al. Mutations in the UBIAD1 gene on chromosome short arm 1, region 36, cause Schnyder crystalline corneal dystrophy. *Invest Ophthalmol. Vis. Sci.* **48**, 5007–5012 (2007).
25. Jo, Y. et al. Schnyder corneal dystrophy-associated UBIAD1 inhibits ER-associated degradation of HMG CoA reductase in mice. *eLife* **8**, <https://doi.org/10.7554/eLife.44396> (2019).
26. Stossel, T. P. The discovery of statins. *Cell* **134**, 903–905 (2008).
27. Virani, S. S. et al. Heart disease and stroke statistics-2021 update: a report from the American Heart Association. *Circulation* **143**, e254–e743 (2021).
28. Reihner, E. et al. Influence of pravastatin, a specific inhibitor of HMG-CoA reductase, on hepatic metabolism of cholesterol. *N. Engl. J. Med.* **323**, 224–228 (1990).
29. Kita, T., Brown, M. S. & Goldstein, J. L. Feedback regulation of 3-hydroxy-3-methylglutaryl coenzyme A reductase in livers of mice treated with mevinolin, a competitive inhibitor of the reductase. *J. Clin. Invest.* **66**, 1094–1100 (1980).
30. Schonewille, M. et al. Statins increase hepatic cholesterol synthesis and stimulate fecal cholesterol elimination in mice. *J. Lipid Res.* **57**, 1455–1464 (2016).
31. Engelking, L. J. et al. Severe facial clefting in Insig-deficient mouse embryos caused by sterol accumulation and reversed by lovastatin 1. *J. Clin. Invest.* **116**, 2356–2365 (2006).
32. Goldberg, I. J. et al. Lack of effect of lovastatin therapy on the parameters of whole-body cholesterol metabolism. *J. Clin. Invest.* **86**, 801–808 (1990).
33. Jun, D. J. et al. Schnyder corneal dystrophy-associated UBIAD1 is defective in MK-4 synthesis and resists autophagy-mediated degradation. *J. Lipid Res.* **61**, 746–757 (2020).
34. Mukherjee, S. et al. Synthetic antibodies against BRIL as universal fiducial marks for single-particle cryoEM structure determination of membrane proteins. *Nat. Commun.* **11**, 1598 (2020).
35. Tsutsumi, N. et al. Structure of human Frizzled5 by fiducial-assisted cryo-EM supports a heterodimeric mechanism of canonical Wnt signaling. *eLife* **9**, <https://doi.org/10.7554/eLife.58464> (2020).
36. Jo, Y. et al. Enhanced ER-associated degradation of HMG CoA reductase causes embryonic lethality associated with Ubiad1 deficiency. *eLife* **9**, <https://doi.org/10.7554/eLife.54841> (2020).
37. Huang, H. et al. Structure of a membrane-embedded prenyltransferase homologous to UBIAD1. *PLoS Biol.* **12**, e1001911 (2014).
38. Cheng, W. & Li, W. Structural insights into ubiquinone biosynthesis in membranes. *Science* **343**, 878–881 (2014).

39. Li, W. Bringing bioactive compounds into membranes: the UbiA superfamily of intramembrane aromatic prenyltransferases. *Trends Biochem. Sci.* **41**, 356–370 (2016).
40. Brown, M. S., Radhakrishnan, A. & Goldstein, J. L. Retrospective on cholesterol homeostasis: the central role of Scap. *Annu. Rev. Biochem.* **87**, 783–807 (2018).
41. Pfeffer, S. R. NPC intracellular cholesterol transporter 1 (NPC1)-mediated cholesterol export from lysosomes. *J. Biol. Chem.* **294**, 1706–1709 (2019).
42. Qi, X. & Li, X. Mechanistic insights into the generation and transduction of Hedgehog signaling. *Trends Biochem. Sci.* **45**, 397–410 (2020).
43. Yang, T. et al. Crucial step in cholesterol homeostasis: sterols promote binding of SCAP to INSIG-1, a membrane protein that facilitates retention of SREBPs in ER. *Cell* **110**, 489–500 (2002).
44. Li, X. et al. Structure of human Niemann-Pick C1 protein. *Proc. Natl Acad. Sci. USA* **113**, 8212–8217 (2016).
45. Qi, X., Schmiede, P., Coutavas, E., Wang, J. & Li, X. Structures of human Patched and its complex with native palmitoylated sonic hedgehog. *Nature* **560**, 128–132 (2018).
46. Qi, X., Schmiede, P., Coutavas, E. & Li, X. Two Patched molecules engage distinct sites on Hedgehog yielding a signaling-competent complex. *Science*, <https://doi.org/10.1126/science.aas8843> (2018).
47. Zhang, Y. et al. Structural basis for cholesterol transport-like activity of the hedgehog receptor patched. *Cell* **175**, 1352–1364 e1314 (2018).
48. Cannac, F. et al. Cryo-EM structure of the Hedgehog release protein dispatched. *Sci. Adv.* **6**, eaay7928 (2020).
49. Kober, D. L. et al. Scap structures highlight key role for rotation of intertwined luminal loops in cholesterol sensing. *Cell* **184**, 3689–3701 e3622 (2021).
50. Yan, R. et al. A structure of human Scap bound to Insig-2 suggests how their interaction is regulated by sterols. *Science* **371**, <https://doi.org/10.1126/science.abb2224> (2021).
51. Long, T. et al. Structural basis for itraconazole-mediated NPC1 inhibition. *Nat. Commun.* **11**, 152 (2020).
52. Long, T., Liu, Y., Qin, Y., DeBose-Boyd, R. A. & Li, X. Structures of dimeric human NPC1L1 provide insight into mechanisms for cholesterol absorption. *Sci. Adv.* **7**, <https://doi.org/10.1126/sciadv.abh3997> (2021).
53. Wang, Q. et al. Dispatched uses Na<sup>+</sup> flux to power release of lipid-modified Hedgehog. *Nature* **599**, 320–324 (2021).
54. Morales-Perez, C. L., Noviello, C. M. & Hibbs, R. E. Manipulation of subunit stoichiometry in heteromeric membrane proteins. *Structure* **24**, 797–805 (2016).
55. Tsutsumi, N. et al. Structure of human Frizzled5 by fiducial-assisted cryo-EM supports a heterodimeric mechanism of canonical Wnt signaling. *eLife* **9**, e58464 (2020).
56. Wang, Q. et al. A combination of human broadly neutralizing antibodies against Hepatitis B virus HBsAg with distinct epitopes suppresses escape mutations. *Cell Host Microbe* **28**, 335–349 e336 (2020).
57. Mastrorade, D. N. Automated electron microscope tomography using robust prediction of specimen movements. *J. Struct. Biol.* **152**, 36–51 (2005).
58. Zheng, S. Q. et al. MotionCor2: anisotropic correction of beam-induced motion for improved cryo-electron microscopy. *Nat. Methods* **14**, 331–332 (2017).
59. Rohou, A. & Grigorieff, N. CTFIND4: Fast and accurate defocus estimation from electron micrographs. *J. Struct. Biol.* **192**, 216–221 (2015).
60. Wagner, T. et al. SPHIRE-crYOLO is a fast and accurate fully automated particle picker for cryo-EM. *Commun. Biol.* **2**, 218 (2019).
61. Punjani, A., Rubinstein, J. L., Fleet, D. J. & Brubaker, M. A. cryoSPARC: algorithms for rapid unsupervised cryo-EM structure determination. *Nat. Methods* **14**, 290–296 (2017).
62. Zivanov, J. et al. New tools for automated high-resolution cryo-EM structure determination in RELION-3. *eLife* **7**, <https://doi.org/10.7554/eLife.42166> (2018).
63. Jumper, J. et al. Highly accurate protein structure prediction with AlphaFold. *Nature* **596**, 583–589 (2021).
64. Waterhouse, A. et al. SWISS-MODEL: homology modelling of protein structures and complexes. *Nucleic acids Res.* **46**, W296–W303 (2018).
65. Emsley, P. & Cowtan, K. Coot: model-building tools for molecular graphics. *Acta Crystallogr. Sect. D. Biol. Crystallogr.* **60**, 2126–2132 (2004).
66. Adams, P. D. et al. PHENIX: a comprehensive Python-based system for macromolecular structure solution. *Acta Crystallogr. Sect. D. Biol. Crystallogr.* **66**, 213–221 (2010).
67. Murshudov, G. N. et al. REFMAC5 for the refinement of macromolecular crystal structures. *Acta Crystallogr. Sect. D. Biol. Crystallogr.* **67**, 355–367 (2011).
68. Chen, V. B. et al. MolProbity: all-atom structure validation for macromolecular crystallography. *Acta Crystallogr. Sect. D. Biol. Crystallogr.* **66**, 12–21 (2010).
69. Pettersen, E. F. et al. UCSF Chimera—a visualization system for exploratory research and analysis. *J. Comput. Chem.* **25**, 1605–1612 (2004).
70. Pettersen, E. F. et al. UCSF ChimeraX: Structure visualization for researchers, educators, and developers. *Protein Sci.* **30**, 70–82 (2021).
71. Mosley, S. T., Brown, M. S., Anderson, R. G. & Goldstein, J. L. Mutant clone of Chinese hamster ovary cells lacking 3-hydroxy-3-methylglutaryl coenzyme A reductase. *J. Biol. Chem.* **258**, 13875–13881 (1983).

## Acknowledgements

We thank D. Stoddard at the UT Southwestern Cryo-EM Facility (funded in part by the CPRIT Core Facility Support Award RP170644) for data collection, L. Beatty for help with tissue culture and M. Brown, J. Goldstein for discussion during manuscript preparation. We thank A. Kosiakoff and S. Mukherjee for providing the plasmid for anti-BRIL Fab expression. This work was supported by the Endowed Scholars Program in Medical Science of UT Southwestern Medical Center, Welch Foundation (I-1957, to X.L.) and NIH grant P01 HL160487, P01 HL020948, R01 GM134700 (to R.D.B. and X.L.). X.Q. is a recipient of DDBrown Fellowship of Life Sciences Research Foundation. X.L. is a Damon Runyon-Rachleff Innovator supported by the Damon Runyon Cancer Research Foundation (DRR-53S-19) and a Rita C. and William P. Clements Jr. Scholar in Biomedical Research at UT Southwestern Medical Center.

## Author contributions

R.D.B. and X.L. conceived the project and designed the research with H.C., X.Q. H.C. and X.Q. performed biochemical studies and carried out cryo-EM experimentation. H.C., X.Q., and L.D. screened the antibody. H.C., R.A.F., M.M.S. performed functional characterization experiments. X.Q. built the initial models and refined the structures. All of the authors analyzed the data and contributed to manuscript preparation. R.D.B. and X.L. wrote the manuscript.

## Competing interests

The authors declare no competing interests.

## Additional information

**Supplementary information** The online version contains supplementary material available at <https://doi.org/10.1038/s41467-022-32025-5>.

**Correspondence** and requests for materials should be addressed to Russell A. DeBose-Boyd or Xiaochun Li.

**Peer review information** *Nature Communications* thanks Benjamin Orlando for their contribution to the peer review of this work.

**Reprints and permission information** is available at <http://www.nature.com/reprints>

**Publisher's note** Springer Nature remains neutral with regard to jurisdictional claims in published maps and institutional affiliations.

**Open Access** This article is licensed under a Creative Commons Attribution 4.0 International License, which permits use, sharing, adaptation, distribution and reproduction in any medium or format, as long as you give appropriate credit to the original author(s) and the source, provide a link to the Creative Commons license, and indicate if changes were made. The images or other third party material in this article are included in the article's Creative Commons license, unless indicated otherwise in a credit line to the material. If material is not included in the article's Creative Commons license and your intended use is not permitted by statutory regulation or exceeds the permitted use, you will need to obtain permission directly from the copyright holder. To view a copy of this license, visit <http://creativecommons.org/licenses/by/4.0/>.

© The Author(s) 2022